AIAA JOURNAL
Vol. 47, No. 3, March 2009

Experimental and Numerical Study of Forward Flight Aerodynamics of Insect Flapping Wing

Hiroto Nagai*
Kyushu Institute of Technology, Kitakyushu 804-8550, Japan
Koji Isogai† and Tatsumi Fujimoto‡
Nippon Bunri University, Oita 870-0397, Japan
and
Toshiyuki Hayase§
Tohoku University, Sendai 980-8577, Japan

DOI: 10.2514/1.39462

Experimental and numerical studies are conducted on the aerodynamic characteristics of a flapping wing of an insect in forward flight. Unsteady aerodynamic forces and flow patterns are measured using a dynamically scaled mechanical model in a water tunnel. The design of the model is based on the flapping wing of a bumblebee. The forces and flow patterns are also computed using a three-dimensional Navier–Stokes code. Comparisons between the experimental and numerical results show good agreement in the time histories of aerodynamic forces and flow patterns in both hovering and forward flight. Aerodynamic mechanisms of a flapping wing in forward flight, such as delayed stall, rotational effect, and wake capture are examined in detail. The results indicate that these aerodynamic mechanisms had an effect on the aerodynamic characteristics of the flapping wing in forward flight; however, these mechanisms function differently during the up- and downstroke, for different stroke plane angles, and for different advance ratios.

Nomenclature

b	=	semichord length at 2/3 semispan length as a reference length
C_F, C_L, C_T	=	normal fluid force, lift, and thrust coefficients
C_P	=	power coefficient
c_z	=	sectional force coefficient normal to stroke plane
F_n	=	normal force
f	=	flapping frequency
J	=	advance ratio ($=U_0/V_0$)
k	=	reduced frequency
L	=	lift
l_r	=	spanwise length from flapping axis to reference chord
P	=	power
Re	=	Reynolds number
r^*	=	nondimensional spanwise location
T	=	thrust
t^*	=	nondimensional time ($=ft$)
U_0	=	forward velocity
V_0	=	reference velocity ($=2\pi f\phi_0 l_r$)
V_{in}	=	relative inflow velocity
α	=	effective angle of attack
η	=	propulsive efficiency
θ, θ_0	=	feathering angle and amplitude of feathering angle
τ_a	=	rotational acceleration time
τ_r, τ_t	=	rotational time and reversal time
ϕ	=	flapping angle and amplitude of flapping angle
ψ	=	stroke plane angle
ω_y^*	=	nondimensional vorticity about y-axis

Superscripts

*	=	nondimensional parameter
-	=	time-averaged (during one cycle) value

Received 29 June 2008; revision received 18 November 2008; accepted for publication 24 November 2008.

*Postdoctoral Fellow, Laboratory of Spacecraft Environment Interaction Engineering; nagai@mech.kyutech.ac.jp. Member AIAA.
†Professor, Department of Aeronautics and Astronautics; isogai@nbu.ac.jp. Associate Fellow AIAA.
‡Professor, Department of Aeronautics and Astronautics; fujimotm@nbu.ac.jp. Senior Member AIAA.
§Professor, Institute of Fluid Science; hayase@ifs.tohoku.ac.jp.

I. Introduction

MICRO air vehicles (MAVs), which are handheld unmanned aircraft, are expected to be used for rescue, surveillance, exploration, and reconnaissance missions. The flapping flight of an insect has drawn attention as a good candidate for designing MAVs. Many insects have unique flying capabilities, namely, abilities to hover and turn abruptly, in addition to usual cruise flight. Many experimental and numerical studies have clarified the aerodynamic mechanisms of the flapping flight of insects: *delayed stall* [1–5], which is a main contribution to aerodynamic forces due to a leading-edge vortex attached to the wing surface; *rotational effect* [6–9], which results in additional lift during a feathering rotation; *wake capture* [6,8,10], which is the interaction between the wing and the wake induced in the previous stroke; and *clap and fling* [11,12], which is the interaction between the left and right wings.

Because of their very small size and high flapping frequency, direct measurements of the unsteady aerodynamic forces and flow patterns around insects are difficult. In experimental approaches, dynamically scaled mechanical models have provided reliable and significant data on unsteady aerodynamic forces and flow patterns around flapping wings. They have proved to be a powerful tool in the investigation of the aerodynamic mechanisms of flapping wings. Birch and Dickinson [4,10], Sane and Dickinson [5,7], Dickinson et al. [6], Lehmann et al. [11], and Birch et al. [13] have conducted measurements of unsteady aerodynamic forces and flow visualization in an oil tank using a dynamically scaled mechanical model based on a fruit fly. They have clarified the aerodynamic mechanisms of flapping wings in hovering flight. Measurements of unsteady aerodynamic forces of tandem wings based on a dragonfly have been

conducted by Maybury and Lehmann to investigate the flow interaction between the forewings and hind wings using a mechanical model submerged in mineral oil [14]. Such measurements have also been conducted in water by Isogai et al. [15] and Yamamoto and Isogai [16]. The previous studies of force measurements with scaled models have been conducted in still fluids, which simulate only a hovering flight. Recently, Dickson and Dickinson [17] have conducted measurements of aerodynamic forces using their scaled mechanical model translated horizontally in an oil tank with a wing revolving at a constant angular velocity; they have investigated the effect of advance ratio on delayed stall. However, experimental simulations of a flapping wing in forward flight, in which the rotational effect and wake capture are also included, have not been conducted yet.

Numerical simulations using computational fluid dynamics (CFD) have been a powerful and important tool for investigating the aerodynamics of insect flight and developing MAVs. The aerodynamics of flapping wings in forward flight have been studied mainly by numerical simulations [18–20]. However, although the results of numerical simulations have been validated for hovering flight [8,9,15,16,19–23] compared with the experimental data described previously, numerical results for forward flight have not been validated because of a lack of experimental data in forward flight.

In this study, we conduct experimental and numerical simulations of a flapping wing of an insect in forward flight. We also investigate the aerodynamic mechanisms of a flapping wing in forward flight, such as delayed stall, rotational effect, and wake capture. Unsteady aerodynamic forces and flow patterns around the wing are measured using a dynamically scaled mechanical model placed in a water tunnel, which simulates hovering and forward flight of insects. The design of the model is based on the flapping wing of a bumblebee, *Bombus terrestris*. The experimental results are compared with the numerical results computed using the three-dimensional Navier–Stokes code. We also investigate the effects of the advance ratio and stroke plane angle on the aerodynamic characteristics of the flapping wing in forward flight.

II. Materials and Methods

A. Motion Kinematics of a Flapping Wing

Three orthogonal coordinate systems of a flapping wing are employed, as shown in Fig. 1. The origin O is at the base of the right wing, the Z direction is vertically downward, and the X axis is in the direction of the forward flight; $OXYZ$ makes a right-handed Cartesian coordinate system. The z axis coincides with the flapping axis; therefore, the x-y plane coincides with the stroke plane. Although the stroke plane is horizontal in hovering flight, it is tilted at an angle ψ around the Y axis in forward flight. The coordinate system $o_w x_w y_w z_w$ is fixed with the right wing and rotates together with the wing. The y_w axis coincides with the feathering axis of the wing, the z_w axis is parallel to the wing chord direction, and the direction of the x_w axis is from the dorsal to the ventral side. The flapping angle ϕ is defined as the angle between the y_w axis and the y axis, and the feathering angle θ is defined as the angle between the z_w axis and the z axis.

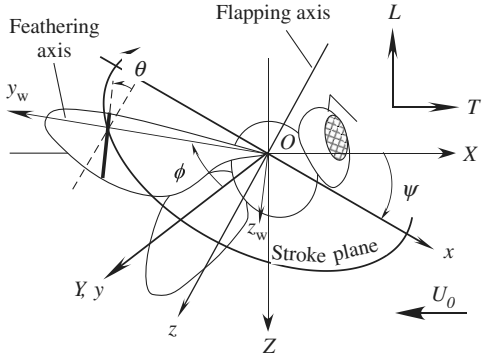

Fig. 1 Three-dimensional coordinate systems of a flapping wing.

The aerodynamic force acting on the wing is divided into a normal force F_n and a tangential force F_t. It is also divided into a vertical component, lift L, and a horizontal component, thrust T. The lift and thrust are related to F_n and F_t as follows:

$$\begin{pmatrix} L \\ T \end{pmatrix} = \begin{pmatrix} \cos\psi & -\sin\psi \\ -\sin\psi & -\cos\psi \end{pmatrix} \begin{pmatrix} \cos\phi\cos\theta & \cos\phi\sin\theta \\ -\sin\theta & \cos\theta \end{pmatrix} \begin{pmatrix} F_n \\ F_t \end{pmatrix} \tag{1}$$

We employed simple trapezoidal-type motion kinematics of the flapping wing, which has been simplified on the basis of the observed data for the bumblebee by Dudley and Ellington [24]. The time histories of its angular velocity are represented as a trapezoidal function, as shown in Fig. 2. The flapping motion can be divided into two phases: a flapping translational phase and a reversal phase. In the flapping translational phase, the wing moves at a constant flapping velocity. In the reversal phase, the wing decelerates and accelerates at a constant rate around the flapping reversal. The duration of the reversal phase is denoted by a reversal time τ_t, which is nondimensionalized by the flapping period. The feathering motion can also be divided into two phases: a feathering translational phase and a rotational phase. The wing moves at a constant angle of attack in the feathering translational phase; then, the wing rotates around the feathering axis in the rotational phase. The time duration of the rotational phase is denoted by a nondimensional time τ_r, and the rotational acceleration time of the feathering motion is denoted by τ_a. In this study, the parameters of motion kinematics were determined as follows: $\tau_t = 0.2$, $\tau_r = 0.3$, and $\tau_a = \tau_r/4$. These parameters were estimated using the observed data for various insects [24,25]. As shown in Fig. 2b, the waveform of feathering motion is symmetrical with respect to the reversal points ($t^* = 0$ and 0.5), and it is referred to as *symmetrical motion* [6].

B. Dynamically Scaled Mechanical Model for Force Measurement

We used a dynamically scaled mechanical model of a flapping wing for measurements of unsteady aerodynamic forces. The scaled mechanical apparatus is illustrated in Fig. 3. The flapping and feathering motions were driven by two stepping motors. The two motions were controlled independently using a controller. The accuracy of the wing motions was confirmed by video images (the maximum error in the angle was 0.09% and the maximum error in the period was 0.3%). The motor for flapping motion was connected to the flapping axis through gears. The motor for feathering motion was

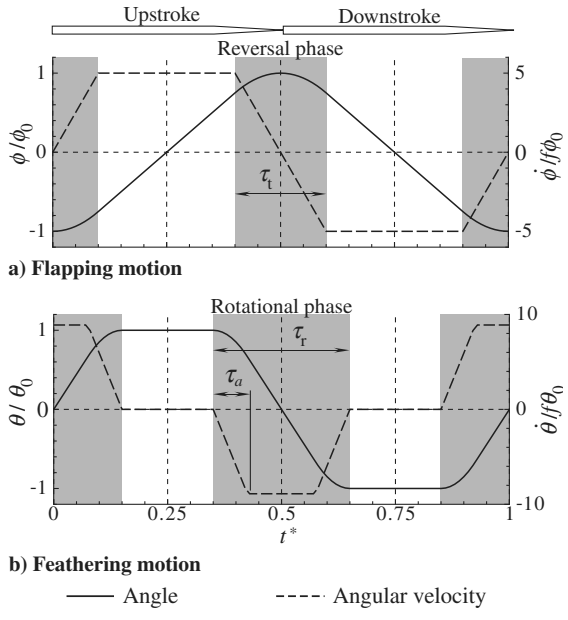

Fig. 2 Time histories of angle and angular velocity of wing kinematics.

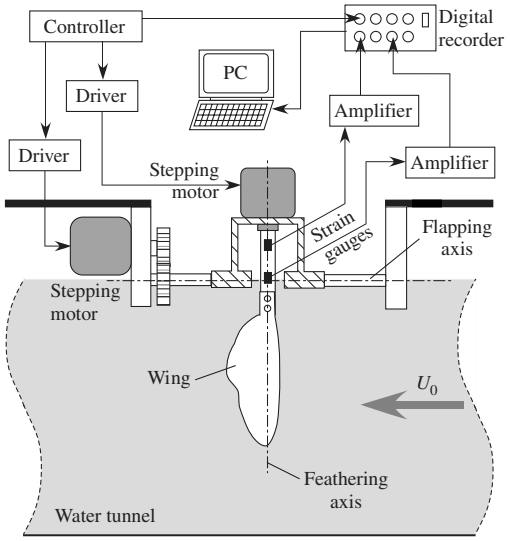

Fig. 3 Dynamically scaled mechanical model for force measurement.

placed on a box fixed to the flapping axis; therefore, the motor rotated with the flapping motion. A rectangular beam ran from the motor for feathering motion to the wing base, passing through the box.

The rectangular beam was used as a force/torque transducer and mounted two sets of strain gauges. The set of strain gauges was placed on the two sides of the beam and wired to form a two-active gauge method that can measure a bending moment. Therefore, the rectangular beam can measure the bending moments at the two different locations of the beam. Although it was difficult to measure the distribution of fluid forces on the wing, we could calculate the total force acting on the wing from the difference between the bending moments at the two locations [16]. The resultant force acting on the wing F is calculated by

$$F = (M_2 - M_1)/d \tag{2}$$

where M_1 and M_2 are the bending moments at the two locations measured by the strain gauges, and d is the distance between the two locations with the strain gauges. The force/torque transducer had a nonlinearity of less than 0.07%. The signals from the force/torque transducer were processed through a signal conditioner/amplifier and filtered using a low-pass filter with a cutoff frequency of 10 Hz. The filtered signals were input into a data acquisition device. In addition, a timing signal from the motor controller was simultaneously input into the data acquisition device to relate the force data to the flapping kinematics. The force data were recorded in eight flapping cycles (7th–14th) in hovering flight and in seven flapping cycles (3rd–9th) in forward flight. We confirmed that a similar aerodynamic force waveform appeared during each cycle. Finally, the averaged force data of a cycle were obtained.

A normal force acting on the wing surface and a torque around the flapping axis were measured in our experiments. It is well known that the fluid force tangential to a thin, flat, flapping wing is very small compared with the normal fluid force [6,13]. In addition, the torque around the feathering axis is very small compared with the torque around the flapping axis [9]. The torque around the flapping axis M_t was interpolated using the measured bending moments at the two locations. The aerodynamic power P required for the flapping motion is given by

$$P = M_t\dot{\phi} \tag{3}$$

Note that the measured forces and torques include the gravitational, buoyant, and inertial contributions, in addition to the aerodynamic force and torque. Therefore, we must subtract these unnecessary forces and torques from the measured data. The gravitational and buoyant forces were measured in water at a very slow flapping frequency of 0.01 Hz; the contribution of inertia was measured in air.

The flapping apparatus was placed over a circuit water tunnel (in Nippon Bunri University, Oita, Japan). The size of the water tunnel was 6 m long × 3 m wide, and it had a test section with dimensions of 1.9 m long × 0.75 m wide × 0.38 m high. The water velocity ranged from 0.02 to 0.2 m/s, where the nonuniformity of velocity was less than 2% across the test section of the water tunnel. The water surface reached the flapping axis; then, the height of water was 0.36 m.

The test wing was a thin, flat plate with a span length of 100 mm and a thickness of 1 mm. The edge around the wing was a square shape. To minimize the gravitational and inertial contributions, the test wing was made of an acrylic plate embedded inside an aluminum frame. The planform of the test wing was similar to that of a bumblebee. The bumblebee has two forewings and two hind wings. The hind wings do not move independently and are coupled with the forewings. In this study, we considered both the forewing and hind wing as a single wing, as shown in Fig. 4. The test wing was considered to be a rigid wing because its deformation was very small. In our experiments, the maximum deformation of the wing tip was not more than 1 mm.

Three nondimensional parameters are required for accurate dynamic scaling of the forces and flows obtained via the scaled model: the Reynolds number, reduced frequency, and advance ratio. A reference length b is 15.75 mm, defined as a semichord length at two-thirds the semispan location, at which the bumblebee has the maximum chord length of its forewing. A reference velocity V_0 is defined on the basis of the flapping velocity and is given by

$$V_0 = 2\pi f \phi_0 l_r \tag{4}$$

where l_r is the length from the flapping axis to the reference chord, f is the flapping frequency, and ϕ_0 is the amplitude of flapping motion. In our experiments, the wing base was placed at a distance of 24 mm from the flapping axis; therefore, $l_r = 90.7$ mm, or the nondimensional spanwise location $r^*(=y_w/l)$ is 0.73.

The Reynolds number, reduced frequency, and advance ratio are defined as follows:

$$Re = V_0 b/\nu, \qquad k = 2\pi f b/V_0, \qquad J = U_0/V_0 \tag{5}$$

where ν is the kinematic viscosity and U_0 is the forward velocity. Although the literature [24] shows that the bumblebee changes the amplitudes of the flapping and feathering angles with respect to the advance ratio, the amplitudes of the flapping and feathering motions were fixed at 60 and 45 deg, respectively, in all our simulations; then, $k = 0.166$. The Reynolds number of the bumblebee is 1980, calculated from Eq. (5), based on the literature [24]. Our measurements were conducted in the range $Re = 1800$–4700 because we confirmed that the Reynolds number had a small effect on the aerodynamic characteristics of the flapping wing in this range; then, the flapping frequency was in the range of 0.2–0.5 Hz.

The measured fluid forces and power are nondimensionalized as follows:

$$C_F = F_n/(0.5\rho V_0^2 S), \quad C_L = L/(0.5\rho V_0^2 S), \quad C_T = T/(0.5\rho V_0^2 S) \tag{6}$$

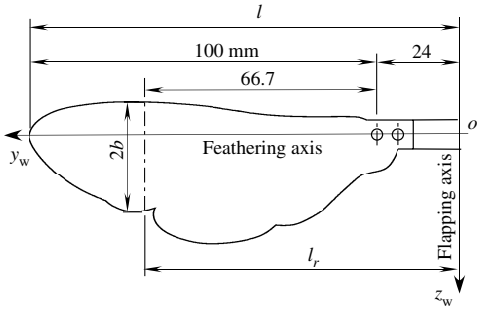

Fig. 4 Planform of test wing.

$$C_P = P/(0.5\rho V_0^3 S) \tag{7}$$

where S is the wing area and ρ is the density of fluid. To evaluate the performance of flapping wings, we defined the efficiency of the flapping wing. Propulsive efficiency is generally defined as

$$\eta = \bar{T}U_0/\bar{P} \tag{8}$$

In hovering or horizontal forward flight, lift does no work on the body of the insect because the body does not move in the vertical direction. However, we considered the ratio of $\bar{C}_L/\bar{C}_P$ as the efficiency of lift in this study.

C. Digital Particle Image Velocimetry

Flow visualization was conducted using stereo digital particle image velocimetry (DPIV). DPIV measurements were performed in the water tunnel using the same dynamically scaled mechanical apparatus. The test wing used for flow visualization was different from that used for the force measurements; it was made entirely of an acrylic plate so that a sheet of light could pass through the wing, and it had a thickness of 2 mm so that the deformation of the wing was very small. The planform was a simple delta shape approximating the planform of the bumblebee, shown in Fig. 4. The two test wings had almost the same area and aspect ratio. By measuring the aerodynamic forces on the two test wings, we confirmed that the difference in their aerodynamic characteristics was not more than 2%. Nylon particles with a mean diameter of 4.1 μm and a density of 1.02 g/cm^3 were used as tracer material. A Nd:YAG laser (Solo III-15, New Wave Research, Inc., United States) was used as a light source; the laser sheet passed horizontally through the side wall of the water tunnel. To visualize the flow pattern of the entire wing, PIV measurements were carried out by applying the laser sheet at 11 different heights. A timing controller (PTU9, LaVision, Germany) was used to synchronize the laser with two double frame digital cameras (Imager Pro X 4M, LaVision). The two cameras were placed below the water tunnel; a mirror inclined at 45 deg was placed in front of the two cameras to reflect flow images through the bottom of the water tunnel. The arrangements of these devices are illustrated in Fig. 5. Image pairs were captured with a time interval of 5 ms. Seven image pairs were recorded in 1 s with a flapping frequency of 0.2 Hz ($Re = 1878$); thus, 35 image pairs were recorded in one flapping cycle. Two cycles (the eighth and ninth cycles) were recorded in one measurement. Two such measurements were carried out under the same condition; as a result, images of four cycles were recorded, which were finally averaged. Image acquisition and processing were performed by LaVision Davis 7.1 software. Each recorded image was processed for obtaining a vector field. In vector field computation, stereo cross-correlation was selected, which used a primary correlation window of 64×64 pixels and a subcorrelation window of 32×32 pixels with a 50% window overlap. This typically yielded 125×125 vectors per PIV image. Once a vector field was calculated, vector validation was applied to eliminate spurious or false vectors. A regional median filter was applied to reject and replace any vectors whose magnitude fell further than two standard deviations from the mean.

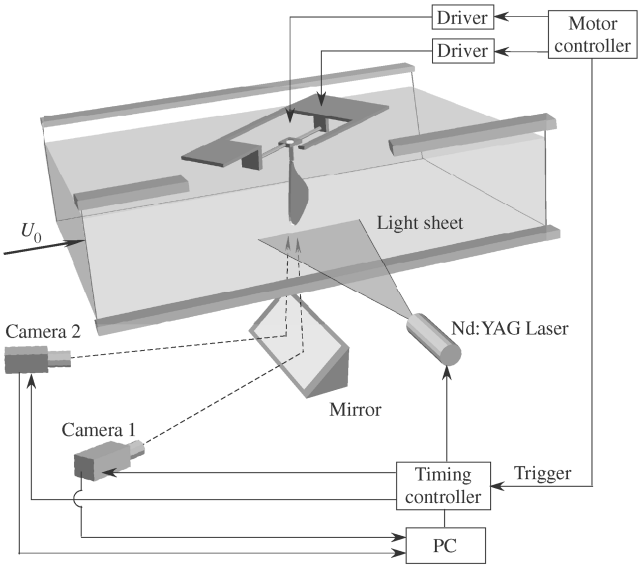

Fig. 5 Arrangement of digital particle image velocimetry system.

D. Numerical Simulation Using Three-Dimensional Navier–Stokes Code

Numerical simulations of a 3-D flapping wing were conducted using the 3-D Navier–Stokes code developed by Isogai et al. [15]. They have validated this code in relation to the time histories of unsteady aerodynamic forces in hovering flight by comparing it with the experimental results obtained using a dynamically scaled mechanical model of a dragonfly in still water [16]. The time-differenced form of the geometric conservation law coupled with the conservation form of the three-dimensional Navier–Stokes (NS) equations was solved at each time step. The implicit time-integration algorithm without inner iteration was used, and the Courant number near the body was taken to be 0.75 so that the time accuracy of the computation was maintained. The total variation diminishing scheme was employed to solve the NS equations. The far-field boundaries were located at a distance of 15 chord lengths in the y direction. At these boundaries, the flow equations were given by the zero-order extrapolation from the inner points. At the $y = 0$ plane, the symmetry conditions were applied. The wing had the same planform as that used in the experiments shown in Fig. 4 but with a zero thickness, unlike that used in the experiments. For all flow computations, the Mach number was assumed to be 0.10, the Reynolds number was 2347, and a no-turbulence model was used because no transition occurs in such a low Reynolds number of the order 10^3.

Three cases were tested for verification of the numerical code. The first case had a grid system of $260 \times 60 \times 35$ with a nondimensional time step of 2.6×10^{-4}. The second case was the same grid system with a fine time step of 1.3×10^{-4}. The third case had a fine grid system of $321 \times 74 \times 42$ with the time step of 2.6×10^{-4}. Figure 6 shows the time histories of lift, thrust, and power coefficients in hovering flight for the three cases. The time histories of the forces in the three cases are in good agreement. The time-averaged values have a difference less than 3% in the three cases. Therefore, we adopted the grid system of $260 \times 60 \times 35$ and the time step of 2.6×10^{-4} in the subsequent calculations. In this grid system, the number of grid points on the upper/lower wing surfaces was 60 in the chordwise direction and 25 in the spanwise direction. The number of grid points in the direction normal to the upper/lower surfaces was 30 in each direction.

III. Validation of Experimental and Numerical Methods

For validation of our experimental and numerical methods, we compare the experimental and numerical results in relation to aerodynamic forces and flow patterns in both hovering and forward flight. First, the time histories of aerodynamic forces are compared between the experimental and numerical results. Figure 6 shows a comparison of the time histories of aerodynamic forces in hovering flight between experimental and numerical results. The experimental and numerical results are in good agreement. In hovering flight, the lift and power have the same waveforms during the up- and downstroke (see Figs. 6a and 6c), whose time-averaged values are positive, because the wing experiences the same flow condition between the up- and downstroke. On the other hand, the waveforms of thrust are the same during the up- and downstroke but are positive and negative, respectively (see Fig. 6b), and the time-averaged value in one flapping cycle is practically zero. In the translational phase (white area in Fig. 6), where the wing moves at a constant flapping velocity and a constant angle of attack, the waveforms obtained by the numerical simulation agree well with those of the experimental

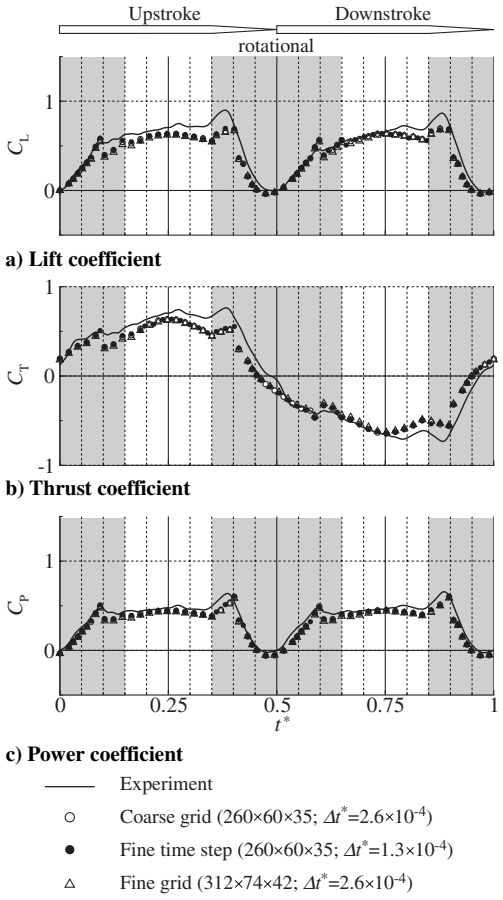

Fig. 6 Verification and validation of time histories of aerodynamic forces in hovering flight.

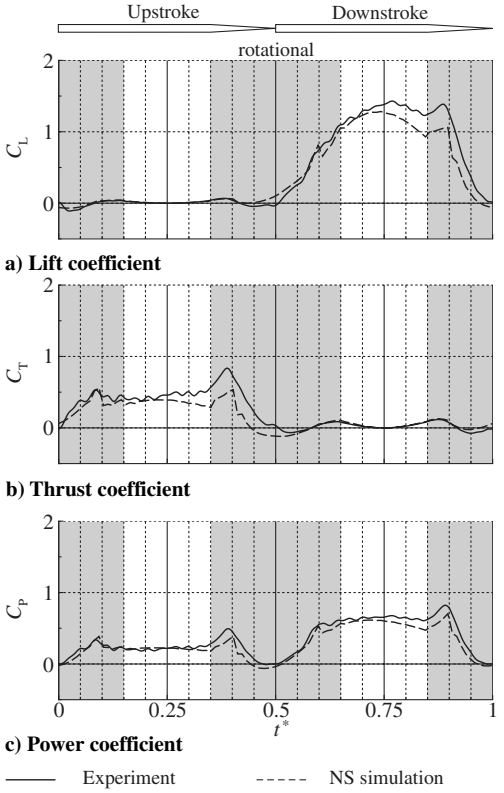

Fig. 7 Comparison of time histories of aerodynamic forces when $J = 0.20$ and $\psi = 45$ deg.

results in C_L, C_T, and C_P. Once the rotational phase begins ($t^* = 0.35$ or 0.85), the fluid forces are enhanced due to the rotational effect; once the deceleration phase begins ($t^* = 0.4$ or 0.9), the fluid forces reduce; once the acceleration phase begins ($t^* = 0.0$ or 0.5), the fluid forces increase rapidly. These trends are observed in the two waveforms of the experimental and numerical results, although slight discrepancies appear in the rotational phase. At the end of the acceleration phase ($t^* = 0.1$ or 0.6), the waveforms of the numerical result have noticeable peaks, which are considered to be due to the discontinuous acceleration at that time, as shown in Fig. 2a.

Figures 7 and 8 show the time histories of the aerodynamic forces in forward flight when $J = 0.20$ and 0.47, respectively, at $\psi = 45$ deg. $J = 0.20$ corresponds to a comparatively slower forward velocity for the bumblebee, that is, 1.7 m/s; $J = 0.47$ corresponds to a comparatively faster forward velocity, that is, 4.0 m/s [24]. It can be seen from Figs. 7 and 8 that the waveforms of the experimental and numerical results in forward flight are in good agreement. In forward flight, the lift is mainly generated during the downstroke, whereas the thrust is mainly obtained during the upstroke.

Next, flow patterns around the flapping wing are compared between the experimental and numerical results. Figures 9a and 9b show the flow patterns in the middle of the downstroke ($t^* = 0.75$) in hovering flight. They are obtained from the experimental and numerical simulation, respectively. The images on the left of Fig. 9 show the three-dimensional distributions of the nondimensional vorticity ω_y^*, in which the images at some wing sections are superimposed (11 sections in PIV; 25 sections in CFD). The images on the right of Fig. 9 show the two-dimensional (X-Z plane) vector distributions of the flow velocity around the section at $r^* = 0.60$, in addition to the distributions of ω_y^*. A comparison between the experimental and numerical results reveals that the distributions of the flow velocity and vorticity agree well qualitatively and quantitatively. In the image on the left of Fig. 9, a counterclockwise leading-edge vortex (light gray) is attached to the wing surface in the range of $r^* = 0$–0.7. The size of the vortex increases further from the wing base, which indicates that the leading-edge vortex forms a conical structure. In the region where $r^* \geq 0.7$, the leading-edge vortex is no longer attached to the wing surface; instead, a clockwise

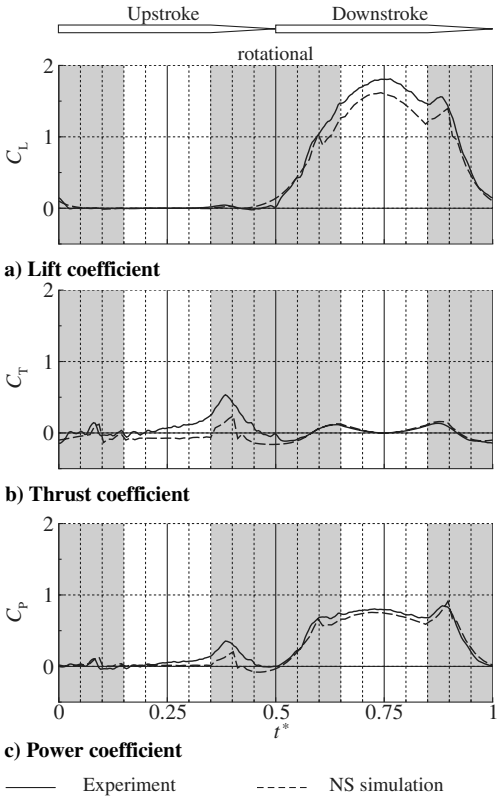

Fig. 8 Comparison of time histories of aerodynamic forces when $J = 0.47$ and $\psi = 45$ deg.

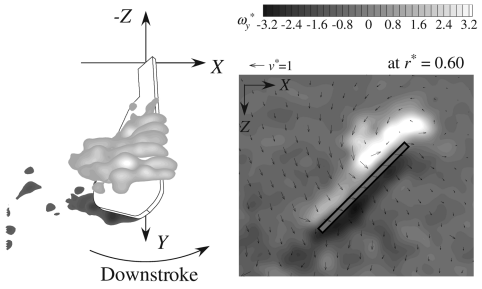

a) Experimental results

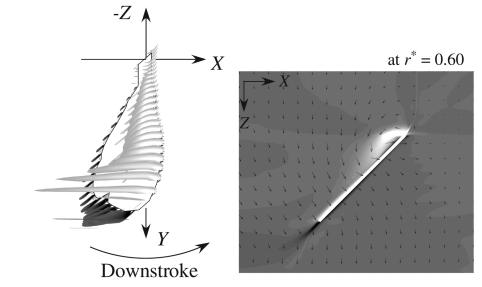

b) Numerical results

Fig. 9 Comparison of vorticity and flow velocity in hovering flight.

trailing-edge vortex (dark gray) is generated. These phenomena are observed in both the experimental and numerical results.

Figures 10a and 10b show the three-dimensional distribution of ω_y^* around the flapping wing in the slower forward flight at $J = 0.20$ obtained by the experimental and numerical simulations, respectively. The images on the left of Fig. 10 show the flow patterns in the middle of the downstroke ($t^* = 0.75$), whereas the ones on the right show the flow patterns in the middle of the upstroke ($t^* = 0.25$). In the downstroke (images on the left in Fig. 10), a counterclockwise leading-edge vortex (light gray) attached to the wing surface is larger than that in hovering flight. On the other hand, in the upstroke (images on the right in Fig. 10), a smaller clockwise leading-edge vortex (dark gray) is attached to the surface near the wing tip. These phenomena are seen in both the experimental and numerical results.

Figures 11a and 11b show the distribution of ω_y^* in the faster forward flight at $J = 0.47$ obtained from the experimental and

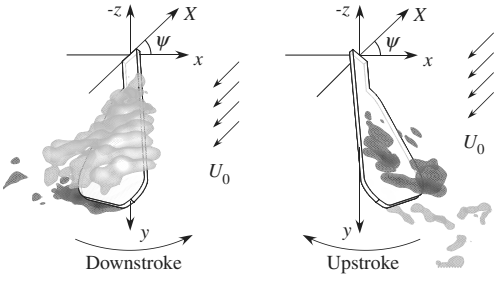

a) Experimental results

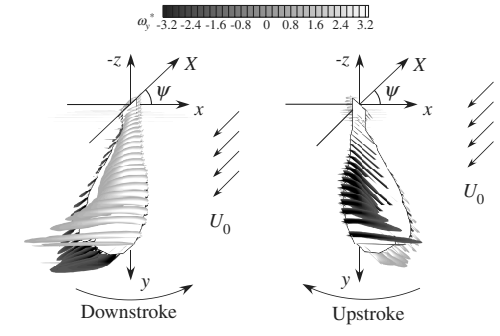

b) Numerical results

Fig. 10 Comparison of vorticity around the wing at $J = 0.20$.

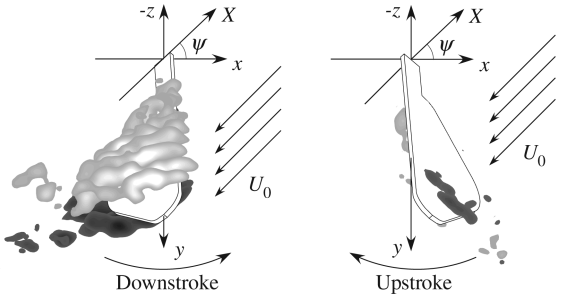

a) Experimental results

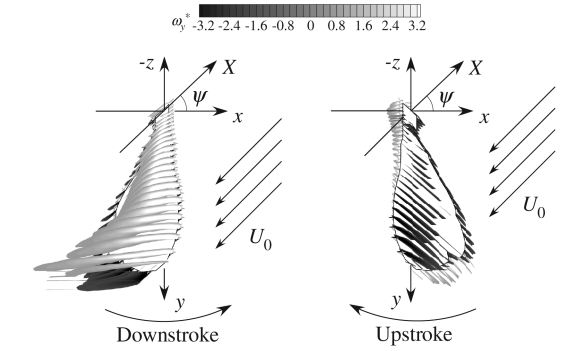

b) Numerical results

Fig. 11 Comparison of vorticity around the wing at $J = 0.47$.

numerical simulations, respectively. As shown in the images on the left of Fig. 11, a much larger counterclockwise leading-edge vortex (light gray) and clockwise trailing-edge vortex (dark gray) appear in the downstroke. On the other hand, a much smaller clockwise leading-edge vortex (dark gray) appears on the upper surface only near the wing tip; in addition, a counterclockwise leading-edge vortex (light gray) appears on the lower surface near the wing base. These phenomena are seen in both the experimental and the numerical results.

Finally, the time-averaged values are compared between the experimental and numerical results. The time-averaged aerodynamic characteristics, with respect to the advance ratio obtained from experiments and numerical simulations, are shown in Fig. 12 for each stroke plane angle. From Figs. 12a–12c and 12e, the time-averaged values of the numerical results are smaller in $\bar{C}_L$, $\bar{C}_T$, $\bar{C}_P$, and η than those of the experimental results. However, the ratio of $\bar{C}_L/\bar{C}_P$ is in very good agreement between the experimental and numerical results (see Fig. 12d). The effects of advance ratio and stroke plane angle on the aerodynamic characteristics (described subsequently in detail) are qualitatively similar between the experimental and numerical results.

Although our experimental and numerical results show good qualitative agreement in both aerodynamic forces and flow patterns in both hovering and forward flight, some quantitative discrepancies exist. It is considered that the main reason of the quantitative discrepancies is the difference of the leading-edge shapes between the experimental and numerical wing models. Whereas the experimental wing model had a square shape of the leading-edge, the numerical one had a sharp leading-edge with a zero thickness. As shown in Fig. 9a, the leading-edge vortex is stretched in front of the leading-edge due to the square edge of the experimental test wing. On the other hand, the leading-edge vortex is generated just at the sharp leading-edge of the numerical test wing as shown in Fig. 9b. As a result, the size of the vortex in the experiment is larger than that in the calculation. Therefore, the time histories of the forces in the numerical simulation are smaller than those in the experiments entirely through the stroke. The time-averaged values shown in Fig. 12 have noticeable discrepancies because the small discrepancies shown in the time histories are integrated through a cycle. Despite the discrepancy of each time-averaged coefficient, the ratio of the coefficients $\bar{C}_L/\bar{C}_P$ is in very good agreement, which indicates the qualitative validity of the numerical results.

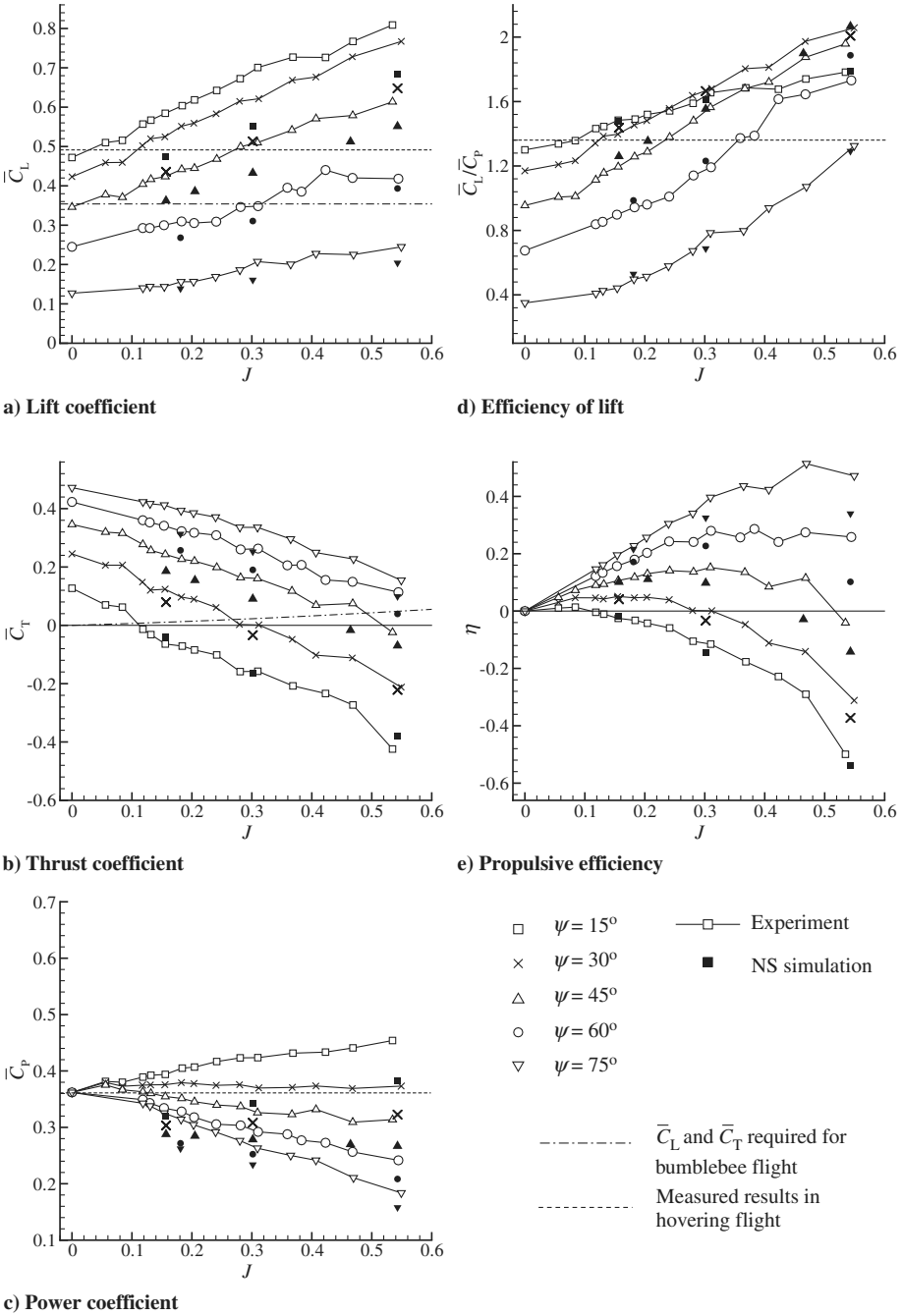

Fig. 12 Plot of aerodynamic characteristics against advance ratio for every stroke plane angle.

The agreements between our experimental and numerical results in hovering and forward flight are as good or better than any other agreement shown in the literature [8,9,15,16,19–23]. Our experimental and numerical results are sufficiently valid to initiate a discussion about the aerodynamic characteristics of a flapping wing in hovering and forward flight.

IV. Results and Discussion

A. Discussion on Time-Averaged Aerodynamic Characteristics

We discuss the time-averaged aerodynamic characteristics shown in Fig. 12 and investigate the effect of advance ratio and stroke plane angle on the aerodynamic characteristics of the flapping wing in forward flight. As shown in Fig. 12a, $\bar{C}_L$ increases with increasing the advance ratio at every stroke plane angle, and $\bar{C}_L$ decreases with an increase in the stroke plane angle for all advance ratios. The dashed line in Fig. 12a indicates the experimental result in hovering flight at $\psi = 0$ deg. Because of the inclination of the stroke plane angle, $\bar{C}_L$ in forward flight is smaller than that in hovering flight at low advance ratios; however, some values are higher at high advance ratios. The dashed-dotted line in Fig. 12a indicates the $\bar{C}_L$ required by the bumblebee to stay aloft [24]. The results indicate that the wings at $\psi = 75$ deg cannot generate enough lift for the bumblebee to stay aloft in the range of $J \leq 0.5$.

As shown in Fig. 12b, $\bar{C}_T$ decreases with an increase in the advance ratio at every stroke plane angle and becomes negative at an advance ratio, which means that the flapping wing generates drag. $\bar{C}_T$ increases with the stroke plane angle for all advance ratios. The dashed-dotted line in Fig. 12b indicates the body drag coefficient for the bumblebee [26]. $\bar{C}_T$ above the dashed-dotted line is required for forward flight of the bumblebee. The results for $J = 0.2$ indicate that the bumblebee can achieve sufficient lift but cannot fly forward at $\psi = 15$ deg; however, it may be able to fly forward but not horizontally at $\psi = 60$ deg. Hence, the bumblebee needs to select an appropriate stroke plane angle with respect to the advance ratio. The stroke plane angle of the bumblebees is not more than 45 deg in the

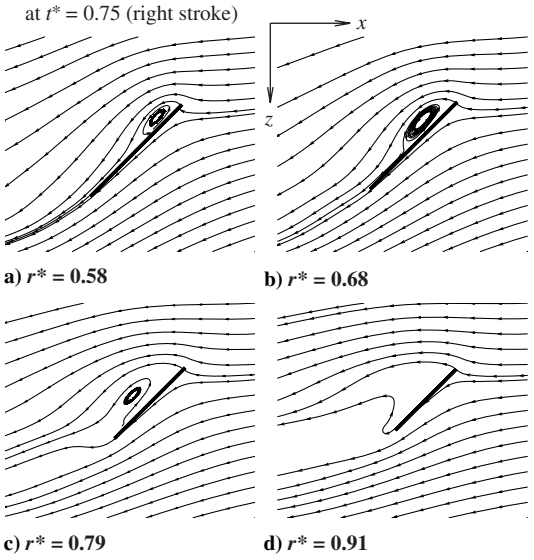

Fig. 13 Instantaneous two-dimensional streamlines around four sections in hovering flight.

range of $J \leq 0.53$ according to the observation [24]. The experimental and numerical results of the flapping wing when $\psi = 45$ deg and $J = 0.53$ indicate that the bumblebee can generate enough lift to stay aloft; however, it falls a little short of the thrust required to carry it in its forward flight. Unlike in this simulation, a bumblebee in fact uses different amplitude of feathering angle between the up- and downstroke and through the advance ratios [24].

As shown in Fig. 12c, $\bar{C}_P$ at $\psi = 15$ deg increases with the advance ratio and is larger than that in hovering flight; $\bar{C}_P$ at $\psi = 30$ deg is almost constant with respect to the advance ratio, and $\bar{C}_P$ at $\psi \geq 45$ deg decreases with an increase in the advance ratio and is smaller than that in hovering flight. As shown in Fig. 12d, $\bar{C}_L/\bar{C}_P$ increases with the advance ratio at every stroke plane angle; in addition, the increase rate of $\bar{C}_L/\bar{C}_P$ with respect to the advance ratio increases with the stroke plane angle. For example, although $\bar{C}_L/\bar{C}_P$ at $\psi = 15$ deg is larger than any other stroke plane angle when $J < 0.25$, it is smaller than that at $\psi = 30$ deg when $J > 0.25$ and that at $\psi = 45$ deg when $J > 0.37$. This fact implies that the flapping wing generates lift more efficiently with a larger stroke plane angle at high advance ratios, benefiting from the freestream. As shown in Fig. 12e, η has a maximum in an advance ratio at every stroke plane angle. The advance ratio with the maximum of η and the maximum value increase with increasing stroke plane angle.

B. Discussion on Flow Conditions

To investigate the cause of the aerodynamic characteristics just described, we will now discuss the flow conditions around the flapping wing in forward flight and investigate the effect of advance ratio on the aerodynamic characteristics. In this section, the numerical results are mainly used because they simplify the investigation of the overall three-dimensional flow around a flapping wing.

Figure 13 shows the two-dimensional instantaneous streamlines around the four wing sections in the middle of the downstroke in hovering flight. Note that the streamlines presented in this paper are expressed as the relative flow against the wing (in the $x_w y_w z_w$ coordinate system). The streamline separated from the leading-edge is reattached to the wing in the range of $r^* = 0$–0.7, forming a vortex bubble (see Fig. 13a). The leading-edge vortex attached to the wing surface enhances the fluid force acting on the wing. The corresponding spanwise distribution of the sectional force coefficient c_z normal to the stroke plane is shown in Fig. 14a. In this figure, it is observed that c_z increases from the wing base up to $r^* = 0.7$. At $r^* = 0.7$, which corresponds to the tip of the hind wing, the reattachment point reaches the trailing edge and the vortex bubble covers the entire upper surface, as shown in Fig. 13b; then, c_z is maximum. At $r^* = 0.7$–0.8, the separated flow from the leading-edge is no longer reattached; however, the vortex remains near the upper surface of the wing (see Fig. 13c); c_z, then, retains its high value in spite of a decrease in the chord length. In the region where $r^* \geq 0.8$, the leading-edge vortex is shed from the wing surface; instead, trailing-edge vortices are generated (see Fig. 13d). Then, the streamline through the leading-edge has a slight curvature, which is similar to the conventional stall occurring on a fixed wing; this results in a decrease in the value of c_z. Figure 14b shows the corresponding instantaneous three-dimensional streamlines through the leading edge. There is a strong spanwise flow in the core of the leading-edge vortex from the wing base to the tip. The path of the spanwise flow is near the leading-edge on the upper surface up to $r^* = 0.7$. Then, it is swept downstream and leaves the upper surface gradually from $r^* = 0.7$; finally, it gets connected to the tip vortex. The presence of the spanwise flow is attributed to the leading-edge vortex attached stably to the wing during a flapping translation [1,4,13]. The spanwise flow is accelerated by a favorable pressure gradient and has a maximum velocity of approximately $v^* = 0.6$ at $r^* = 0.5$. The spanwise flow velocity reaches almost the relative inflow velocity at each wing section. In the region where $r^* \geq 0.5$, the spanwise flow is decelerated by an adverse pressure gradient; then, it is swept downstream away from the wing surface.

Next, we discuss the flowfield around the flapping wing as an example of intermediate forward flight of $J = 0.20$ at $\psi = 45$ deg, where the propulsive efficiency is almost maximum, as shown in Fig. 12e. Figure 15a shows the spanwise distributions of c_z in the middle of the up- and downstroke ($t^* = 0.25$ and 0.75), respectively. As in hovering flight, c_z also has a maximum at approximately $r^* = 0.7$ in the downstroke. The corresponding instantaneous three-dimensional streamlines in the downstroke are shown in Fig. 15b. There is also a strong spanwise flow in the core of the leading-edge vortex. The path of the spanwise flow is totally swept downstream compared with that in hovering flight. The maximum spanwise flow velocity is approximately $v^* = 0.65$ at $r^* = 0.4$. The spanwise flow velocity at $J = 0.20$ also reaches almost the relative inflow velocity at each wing section. On the other hand, the point with the maximum of c_z in the upstroke is at $r^* = 0.8$ (see the dotted line in Fig. 15a), and it moves toward the wing tip compared with that in the downstroke. The corresponding three-dimensional streamlines in the upstroke are shown in Fig. 15c. A weak leading-edge vortex lies only near the wing tip in the upstroke (also shown in Fig. 10a), and a weak spanwise flow exists in the core of the leading-edge vortex from approximately $r^* = 0.5$ to the tip. As a result, aerodynamic force is generated mainly near the wing tip. The strong spanwise flow in the

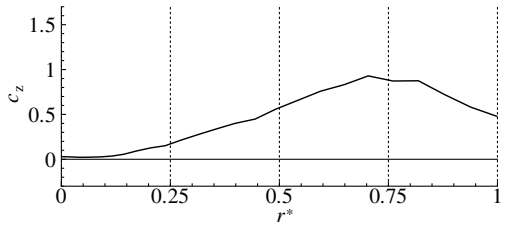

a) Spanwise distribution of c_z

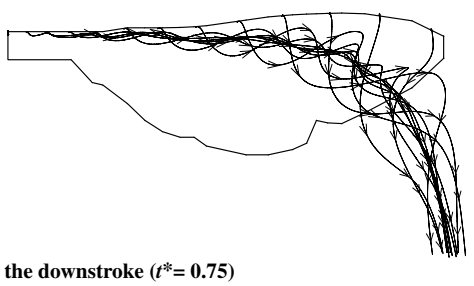

b) In the downstroke (t^*= 0.75)

Fig. 14 Spanwise distribution of aerodynamic force and instantaneous streamlines in hovering flight.

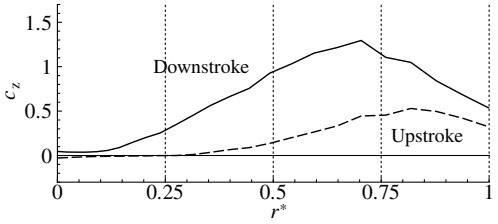

a) Spanwise distribution of c_z

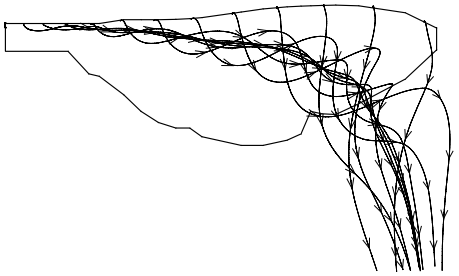

b) In the downstroke (t^* = 0.75)

c) In the upstroke (t^* = 0.25)

Fig. 15 Spanwise distribution of aerodynamic force and the corresponding instantaneous streamlines at $J = 0.20$.

downstroke and the weak spanwise flow in the upstroke also contribute to the stable attachment of the leading-edge vortex to the wing surface during the flapping translation in forward flight. In fact, the stable attachment of the leading-edge vortex in forward flight was observed in the experimental results that were obtained from DPIV measurements. Figure 16 shows the experimental results of the vorticity sequences around the flapping wing at $J = 0.20$ during the translational phases in the up- and downstroke. It is found that the leading-edge vortices are never shed from the wing surface during the flapping translations in forward flight.

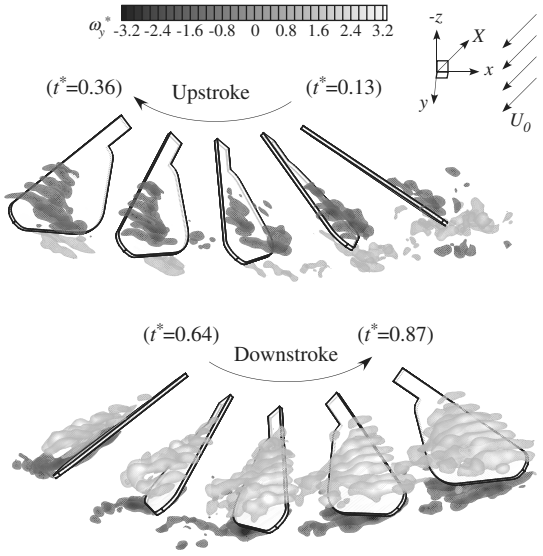

Fig. 16 Experimental results of vorticity sequence around the wing through the up- and downstroke at $J = 0.20$.

The flowfields around the flapping wing at the faster forward flight of $J = 0.47$ are presented here, at which the wing generates a slight thrust (see Fig. 12b). Figure 17a shows the spanwise distributions of c_z in the middle of the up- and downstroke. The maximum of c_z is at approximately $r^* = 0.7$ in the downstroke. The corresponding instantaneous two-dimensional streamlines around some sections are shown in Fig. 18. The streamline separated from the leading edge is reattached at the trailing edge at $r^* = 0.58$ (see Fig. 18a). At $r^* = 0.6$–0.7, the separated flow from the leading edge is no longer reattached. However, the vortex remains near the upper surface of the wing (see Fig. 18b); then, c_z retains its high values. In the region where $r^* \geq 0.8$, the leading-edge vortex is shed from the wing surface and trailing-edge vortices are generated (see Fig. 18c). The corresponding three-dimensional streamlines are shown in Fig. 17b. There is also a strong spanwise flow in the core of the leading-edge vortex in the downstroke at $J = 0.47$, while no spanwise flow appears at the wing base because the forward velocity is predominant compared to the flapping velocity. The path of the spanwise flow is similar to that at $J = 0.20$. The maximum spanwise flow velocity is approximately $v^* = 0.8$ at $r^* = 0.4$. The spanwise flow velocity at $J = 0.47$ also almost corresponds to the relative inflow velocity at each wing section. On the other hand, c_z in the upstroke is negative almost along the wingspan and becomes positive at $r^* \geq 0.8$ (see the dotted line in Fig. 17a). The corresponding two-dimensional streamlines at $r^* = 0.27$ in the middle of the upstroke are shown in Fig. 18d. In this figure, the inflow due to flapping motion is directed from left to right, and the inflow due to forward flight is directed from upper right to lower left. As a result, the net inflow, or the resultant

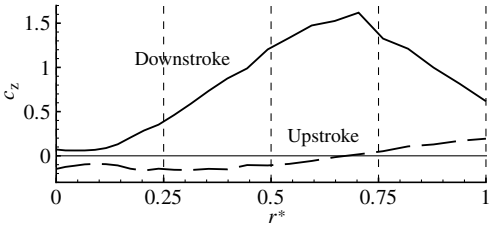

a) Spanwise distribution of c_z

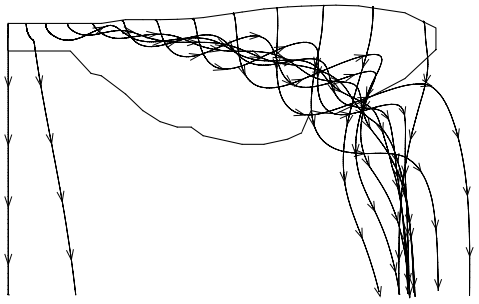

b) In the downstroke (t^* = 0.75)

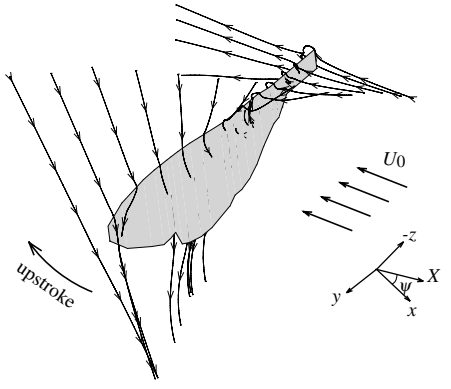

c) In the upstroke (t^* = 0.25)

Fig. 17 Spanwise distribution of aerodynamic force and the corresponding instantaneous streamlines at $J = 0.47$.

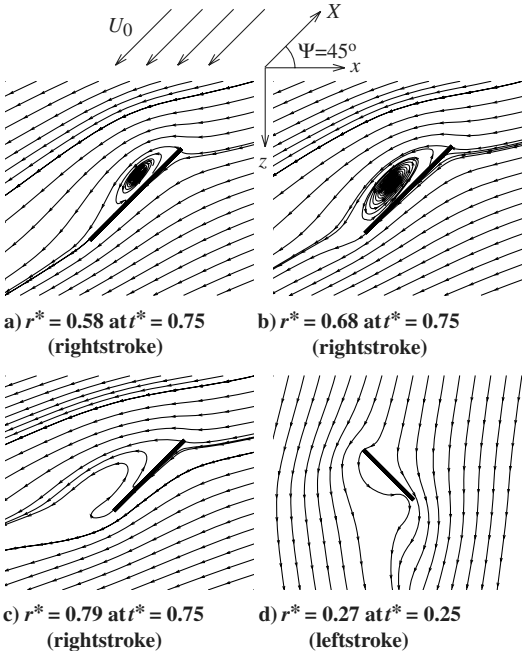

Fig. 18 Instantaneous two-dimensional streamlines at four sections around the wing at $J = 0.47$.

inflow, enters the airfoil section from the upper surface. The corresponding three-dimensional streamlines are shown in Fig. 17c. There is no spanwise flow on the wing, and the inflow direction is changed significantly along the wingspan: right to left at the wing base and upper left to lower right at the wing tip. It is found that the wing experiences a backflow condition near its base.

For a three-dimensional flapping wing, the effective angle of attack is constant along the wingspan in hovering flight because the inflow to the wing is caused only by the flapping motion of the wing. Thus, the effective angle of attack is determined by only the instantaneous feathering angle, and the relative inflow velocity is determined by only the flapping velocity. If the wing moves symmetrically in the up- and downstroke, then it experiences the same inflow condition in the two strokes. On the other hand, the inflow to the wing in forward flight is caused by both the flapping motion of the wing and the forward velocity. Thus, the effective angle of attack and the relative inflow velocity in forward flight are determined by the instantaneous wing motion and attitude, that is, flapping and feathering angles, stroke plane angle, flapping velocity, and forward velocity. Therefore, the inflow conditions in forward flight are variable along the wingspan and differ between the up- and downstroke even if the wing moves symmetrically in both strokes. The spanwise variations of the effective angle of attack in the middle of the up- and downstroke ($t^* = 0.25$ and 0.75) at $\psi = 45$ deg are shown in Fig. 19. Although the effective angle of attack in forward flight is positive all along the span in the downstroke, it changes from negative at the wing base to positive at the wing tip in the upstroke. This indicates the presence of a backflow condition near the wing base in the upstroke. As the advance ratio increases, the variation of α along the span is not changed so much in the downstroke, although it is changed considerably in the upstroke. By increasing the advance ratio, the point at which α changes from negative to positive moves further from the wing base to the wing tip ($r^* = 0.27$ when $J = 0.20$ and $r^* = 0.61$ when $J = 0.47$).

C. Discussion on Time-Varying Aerodynamic Forces

We discuss the time histories of the aerodynamic forces of the flapping wing in forward flight and investigate the effect of advance ratio and stroke plane angle on the aerodynamic forces of the flapping wing. In this section, the experimental results are used for the discussion of the time histories of aerodynamic forces.

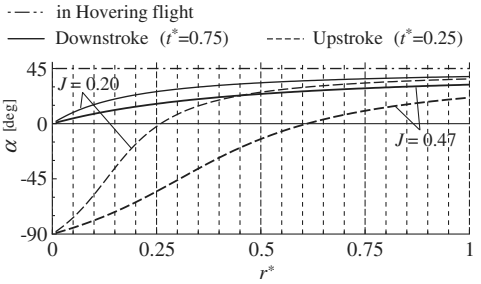

Fig. 19 Effective angle of attack along the wingspan.

Figures 20a and 21a show the time histories of the aerodynamic force coefficient normal to the wing surface at every stroke plane angle when $J = 0.20$ and 0.47, respectively. First, let us discuss the translational phase in forward flight (white areas in the figures). The delayed stall effect is predominant in the translational phase, where the wing moves at a constant flapping velocity and at a constant feathering angle. Although C_F in the upstroke is almost the same at every stroke plane angle, C_F in the downstroke increases with a decrease in the stroke plane angle. As the advance ratio increases, C_F decreases in the upstroke and increases in the downstroke. These tendencies are related mainly to the relative inflow velocity and effective angle of attack. Figures 22a and 22b show the time histories

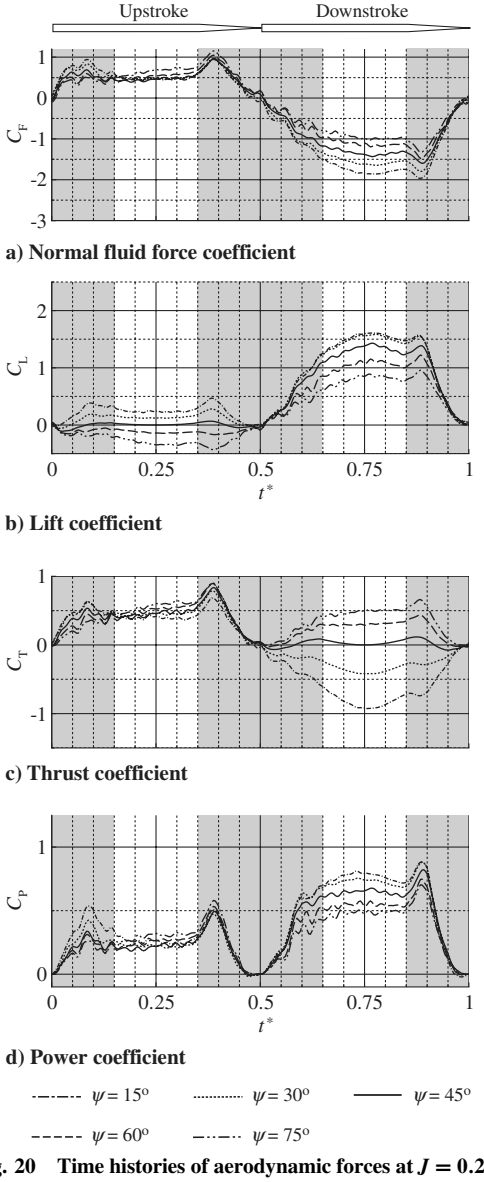

Fig. 20 Time histories of aerodynamic forces at $J = 0.20$.

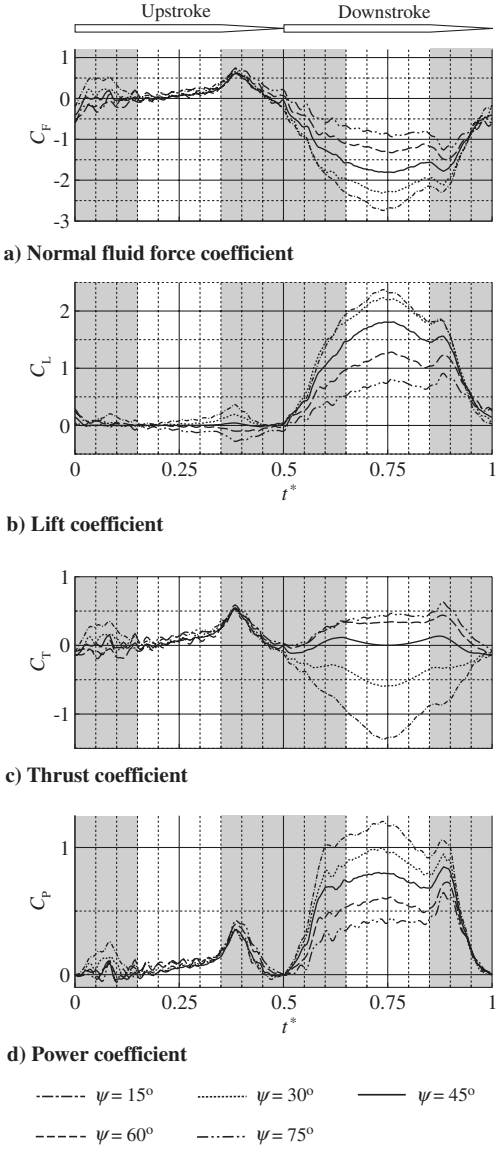

Fig. 21 Time histories of aerodynamic forces at $J = 0.47$.

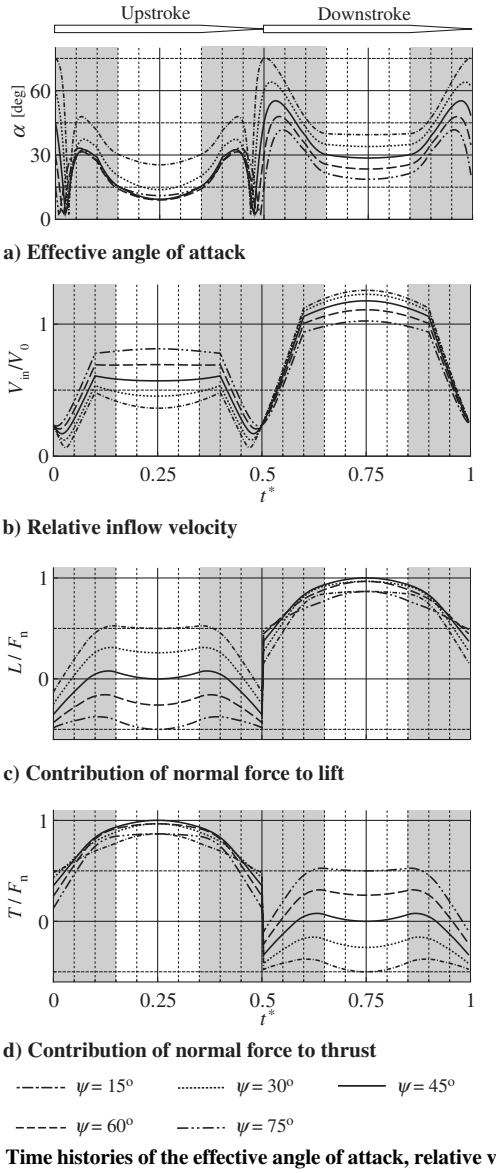

Fig. 22 Time histories of the effective angle of attack, relative velocity, and contribution of normal force to lift and thrust.

of the effective angle of attack and relative inflow velocity at the reference chord ($r^* = 0.73$) when $J = 0.47$ with respect to the stroke plane angle. In the downstroke, both the effective angle of attack and relative inflow velocity increase with a decrease of the stroke plane angle; therefore, C_F increases in the downstroke with a decrease of the stroke plane angle. On the other hand, in the upstroke, the effective angle of attack increases but the relative inflow velocity decreases with a decrease of the stroke plane angle. As a result, C_F in the upstroke is almost unchanged at every stroke plane angle. In the upstroke, although the effective angle of attack is always positive at the reference chord, as shown in Fig. 22a, it is negative near the wing base because of the backflow condition. As a result, the total fluid force acting on the wing is almost zero at $J = 0.47$.

Next, let us discuss the rotational phase in forward flight (gray areas in the figures). As the rotational phase begins, C_F increases rapidly (see $t^* = 0.35$–0.4 or 0.85–0.9 in Figs. 20a and 21a). The increment in C_F due to the rotational effect is similar for different stroke plane angles and for different advance ratios, which is in contrast with the delayed stall effect that has significant differences for different stroke plane angles and advance ratios. This fact indicates that the rotational effect is slightly dependent on the effective angle of attack and advance ratio because the rotational velocity is faster than the flapping and forward velocities in the range of the advance ratio that is experienced by insects. The peaks of C_F due to the rotational effect are larger than the values of C_F in the translational phase at $J = 0.20$. On the other hand, these peaks are smaller than the values of C_F in the translational phase at $J = 0.47$. Because the rotational effect hardly benefits from the forward velocity as compared with the delayed stall effect, the increase in the advance ratio diminishes the importance of the rotational effect in comparison with the delayed stall.

Although no peak of C_F appears in the early downstroke, there is a peak of C_F in the early upstroke (at $t^* = 0.08$), particularly at a smaller stroke plane angle (e.g., case of $\psi = 15$ deg in Fig. 21a). This is attributed to wake capture, which is the interaction between the wing and the wake induced in the previous stroke. The vortices produced in the previous upstroke are swept downstream away from the wing in the early downstroke because the wing in the downstroke moves in the opposite direction of the freestream. As a result, they have a small effect on the wing. On the other hand, because the wing moves together with the freestream in the upstroke, the vortices produced in the previous downstroke seem to remain near the wing in the early upstroke, particularly at a smaller stroke plane angle. Therefore, wake capture is effective on the aerodynamic forces.

Figures 20b, 20c, 21b, and 21c show the time histories of C_L and C_T at $J = 0.20$ and 0.47, respectively. The waveforms of C_L and C_T in the upstroke are significantly different for different stroke plane angles, although the waveforms of C_F in the upstroke are similar at every stroke plane angle. For example, the waveform of C_L in the upstroke is positive at $\psi = 15, 30$, and 45 deg and negative at $\psi = 60$

and 75 deg; the waveform of C_T in the downstroke is positive at $\psi = 45$, 60, and 75 deg and negative at $\psi = 15$ and 30 deg. For obtaining a larger lift and/or thrust, it is necessary to not only increase the normal force but also select an appropriate wing attitude. Let the contributions of the normal force to lift and thrust be represented by L/F_n and T/F_n, respectively, which can be calculated from Eq. (1) using the instantaneous attitude of the wing: the flapping, feathering, and stroke plane angles. Figures 22c and 22d show the time histories of L/F_n and T/F_n, respectively. The waveforms of C_L and C_T can be well explained by the waveforms of L/F_n and T/F_n. It should be noted that the relation shown in Figs. 22c and 22d change significantly when the amplitude of the feathering angle is changed.

Figures 20d and 21d show the time histories of C_P at $J = 0.20$ and 0.47, respectively. The waveforms of C_P and C_F have common features such as the delayed stall, rotational effect, and wake capture. C_P in the upstroke is similar at every stroke plane angle and decreases with increasing the advance ratio. In the downstroke, with increasing the advance ratio, C_P at $\psi = 15$ deg increases considerably because of the remarkable increase in the flapping torque in the downstroke. On the other hand, C_P at $\psi = 75$ deg decreases because of the significant decrease in the effective angle of attack, as shown in Fig. 22b.

V. Conclusions

We have conducted experimental and numerical simulations of the aerodynamic characteristics of a flapping wing of an insect in forward flight. Unsteady aerodynamic forces and flow patterns around the flapping wing based on a bumblebee have been measured using a dynamically scaled mechanical model in a water tunnel and computed using a three-dimensional Navier–Stokes code. Comparisons between experimental and numerical results show good agreement in the time histories of aerodynamic forces and flow patterns in both hovering and forward flight. The good agreement between the experimental and numerical results suggests that our results are sufficiently reliable to discuss the aerodynamics of the flapping wing in forward flight. We have investigated the aerodynamic mechanisms such as delayed stall, rotational effect, and wake capture of the flapping wing in forward flight. The results indicate that these aerodynamic mechanisms have an effect on the aerodynamic characteristics of the flapping wing in forward flight; however, these mechanisms function differently during the up- and downstrokes, for different stroke plane angles, and for different advance ratios. These aerodynamic mechanisms in forward flight are summarized as follows:

1) Delayed stall is still effective in the translational phase of forward flight. The leading-edge vortex is attached stably to the wing during a flapping translation of forward flight, and a spanwise flow exists in the core of the vortex. While the delayed stall effect is increased in the downstroke, it is reduced in the upstroke with an increase in the advance ratio. At a high advance ratio, the leading-edge vortex and the spanwise flow hardly appear during the upstroke; then, the wing experiences a backflow condition near the wing base.

2) The rotational effect is slightly dependent on the advance ratio and stroke plane angle. An increase in the advance ratio diminishes the importance of the rotational effect relative to delayed stall.

3) Wake capture is effective in the early upstroke and less effective in the early downstroke with a smaller stroke plane angle.

Acknowledgments

This study was supported by the Ministry of Education, Culture, Sports, Science, and Technology of Japan under the High-Tech Research Center Promotion Program. The authors acknowledge the support of Yasuhiro Akahoshi and Laboratory of Space Environment Interaction Engineering of Kyushu Institute of Technology.

References

[1] Ellington, C. P., Van den Berg, C., Willmott, A. P., and Thomas, A. L. R., "Leading-Edge Vortices in Insect Flight," *Nature (London)*, Vol. 384, Dec. 1996, pp. 626–630. doi:10.1038/384626a0

[2] Dickinson, M. H., and Götz, K. G., "Unsteady Aerodynamic Performance of Model Wings at Low Reynolds Numbers," *Journal of Experimental Biology*, Vol. 174, No. 1, 1993, pp. 45–64.

[3] Liu, H., Ellington, C. P., Kawachi, K., Van den Berg, C., and Willmott, A. P., "A Computational Fluid Dynamic Study of Hawkmoth Hovering," *Journal of Experimental Biology*, Vol. 201, No. 4, 1998, pp. 461–477.

[4] Birch, J. M., and Dickinson, M. H., "Spanwise Flow and the Attachment of the Leading-edge Vortex on Insect Wings," *Nature (London)*, Vol. 412, Aug. 2001, pp. 729–733. doi:10.1038/35089071

[5] Sane, S. P., and Dickinson, M. H., "The Control of Flight Force by a Flapping Wing: Lift and Drag Production," *Journal of Experimental Biology*, Vol. 204, No. 19, 2001, pp. 2607–2626.

[6] Dickinson, M. H., Lehmann, F.-O., and Sane, S. P., "Wing Rotation and the Aerodynamic Basis of Insect Flight," *Science*, Vol. 284, No. 5422, June 1999, pp. 1954–1960. doi:10.1126/science.284.5422.1954

[7] Sane, S. P., and Dickinson, M. H., "The Aerodynamic Effects of Wing Rotation and a Revised Quasi-steady Model of Flapping Flight," *Journal of Experimental Biology*, Vol. 205, No. 8, 2002, pp. 1087–1096.

[8] Sun, M., and Tang, J., "Unsteady Aerodynamic Force Generation by a Model Fruit Fly Wing in Flapping Motion," *Journal of Experimental Biology*, Vol. 205, No. 1, 2002, pp. 55–70.

[9] Sun, M., and Tang, J., "Lift and Power Requirements of Hovering Flight in Drosophila Virilis," *Journal of Experimental Biology*, Vol. 205, No. 10, 2002, pp. 2413–2427.

[10] Birch, J. M., and Dickinson, M. H., "The Influence of Wing-Wake Interactions on the Production of Aerodynamic Forces in Flapping Flight," *Journal of Experimental Biology*, Vol. 206, No. 13, 2003, pp. 2257–2272. doi:10.1242/jeb.00381

[11] Lehmann, F.-O., Sane, S. P., and Dickinson, M. H., "The Aerodynamic Effects of Wing-Wing Interaction in Flapping Insect Wings," *Journal of Experimental Biology*, Vol. 208, Aug. 2005, pp. 3075–3092. doi:10.1242/jeb.01744

[12] Weis-Fogh, T., "Quick Estimates of Flight Fitness in Hovering Animals, Including Novel Mechanisms for Lift Production," *Journal of Experimental Biology*, Vol. 59, No. 1, 1973, pp. 169–230.

[13] Birch, M. J., Dickson, W. B., and Dickinson, M. H., "Force Production and Flow Structure of the Leading Edge Vortex on Flapping Wings at High and Low Reynolds Numbers," *Journal of Experimental Biology*, Vol. 207, Feb. 2004, pp. 1063–1072. doi:10.1242/jeb.00848

[14] Maybury, W. J., and Lehmann, F.-O., "The Fluid Dynamic of Flight Control by Kinematic Phase Lag Variation Between Two Robotic Insect Wings," *Journal of Experimental Biology*, Vol. 207, Dec. 2004, pp. 4707–4726. doi:10.1242/jeb.01319

[15] Isogai, K., Fujishiro, S., Saitoh, T., Yamasaki, M., and Matsubara, M., "Unsteady Three-Dimensional Viscous Flow Simulation of Dragonfly Hovering," *AIAA Journal*, Vol. 42, No. 10, 2004, pp. 2053–2058. doi:10.2514/1.6274

[16] Yamamoto, M., and Isogai, K., "Measurement of Unsteady Fluid Dynamic Forces for a Mechanical Dragonfly Model," *AIAA Journal*, Vol. 43, No. 12, 2005, pp. 2475–2480. doi:10.2514/1.15899

[17] Dickson, W. B., and Dickinson, M. H., "The Effect of Advance Ratio on the Aerodynamics of Revolving Wing," *Journal of Experimental Biology*, Vol. 207, Nov. 2004, pp. 4269–4281. doi:10.1242/jeb.01266

[18] Wang, J., and Sun, M., "A Computational Study of the Aerodynamics and Forewing-Hindwing Interaction of a Model Dragonfly in Forward Flight," *Journal of Experimental Biology*, Vol. 208, Sept. 2005, pp. 3785–3804. doi:10.1242/jeb.01852

[19] Sun, M., and Wu, J. H., "Aerodynamic Force Generation and Power Requirements in Forward Flight in a Fruit Fly with Modeled Wing Motion," *Journal of Experimental Biology*, Vol. 206, July 2003, pp. 3065–3083. doi:10.1242/jeb.00517

[20] Wu, J., and Sun, M., "Unsteady Aerodynamic Forces and Power Requirements of a Bumblebee in Forward Flight," *Acta Mechanica Sinica*, Vol. 21, No. 3, June 2005, pp. 207–217. doi:10.1007/s10409-005-0039-5

[21] Wang, Z. J., Birch, J. M., and Dickinson, M. H., "Unsteady Forces and Flows in Low Reynolds Number Hovering Flight: Two-Dimensional

Computations vs Robotic Wing Experiments," *Journal of Experimental Biology*, Vol. 207, Dec. 2004, pp. 449–460.
doi:10.1242/jeb.00739

[22] Sun, M., and Lan, S., "A Computational Study of the Aerodynamic Forces and Power Requirements of Dragonfly (Aeschna juncea) Hovering," *Journal of Experimental Biology*, Vol. 207, April 2004, pp. 1887–1901.
doi:10.1242/jeb.00969

[23] Tang, J., Viieru, D., and Shyy, W., "Effects of Reynolds Number and Flapping Kinematics on Hovering Aerodynamics," *AIAA Journal*, Vol. 46, No. 4, 2008, pp. 967–976.
doi:10.2514/1.32191

[24] Dudley, R., and Ellington, C. P., "Mechanics of Forward Flight in Bumblebees, I: Kinematics and Morphology," *Journal of Experimental Biology*, Vol. 148, No. 1, 1990, pp. 19–52.

[25] Ellington, C. P., "The Aerodynamics of Hovering Insect Flight, III: Kinematics," *Philosophical Transactions of the Royal Society of London, Series B: Biological Sciences*, Vol. 305, No. 1122, Feb. 1984, pp. 41–78.
doi:10.1098/rstb.1984.0051

[26] Dudley, R., and Ellington, C. P., "Mechanics of Forward Flight in Bumblebees, II: Quasi-Steady Lift and Power Requirements," *Journal of Experimental Biology*, Vol. 148, No. 1, 1990, pp. 53–88.

K. Anderson
Associate Editor